Lateral stability and wake analysis of tri-foil system pitching in-line

Jiacheng Guo¹, Pan Han², Yu Pan³, Haibo Dong⁴ University of Virginia, Charlottesville, VA, 22903, USA

In recent years, there has been a growing interest in using tandem foils to mimic and study fish swimming, and to inform underwater vehicle design. Though much effort has been put to understanding the propulsion mechanisms of a tandem-foil system, the stability of such a system and the mechanisms for maintaining it remain an open question. In this study, a 3-foil system in an in-line configuration is used towards understanding the hydrodynamics of lateral stability. The foils actively pitch with varying phase. To quantify lateral force oscillation, the standard deviation of the lateral force, σ_V , calculated over one typical flapping cycle is used, to account for the amount of variation in the lateral force experienced by the system of 3 foils. The higher the standard deviation, the more the spread in the lateral force cycle data, the more lateral momentum exchanged between the flow and the foils, and the less stable the system is. Through phase variations, it is found that the lateral force is minimized when the phases of the three foils are approximately, though not exactly, evenly distributed. The least stable system is found to be the one with the foils all in phase. Systems that are more laterally stable are found to tend to have narrower envelopes of regions around the foils with high momentum. Near-wake of the foils, the envelopes of stable systems are also found to have pronounced convergent sections, whereas the envelope of the less stable systems are found to diverge without much interruption. In the far wake, coherent, singular thrust jets, along with orderly 2-S vortices are found to form in the two best performing cases. In less stable cases, the thrust jets are found to be branched. Corresponding to the width of the high-momentum envelopes, lateral jets are found to exist in the gaps between neighboring foils, the strengths of which vary based on stability, with the lateral jets being more pronounced in the less stable cases (cases with high amount of lateral force oscillation). Peak lateral forces are found to coincide with moments of pressure gradient build-up across the foils. The pressure-driven flow near the trailing edge of the foils then creates trailing-edge vortices, and correspondingly, lateral gap flows. Moments of peak and plateau lateral force on an individual foil in the system are found to coincide with the initiation and shedding of trailing-edge vortices, respectively. The formation of trailing-edge vortices, lateral jets and cross-stream flows in gaps are closely intertwined, and all are 1. Indicative of large lateral momentum oscillation, and 2. The results of pressure gradient build-up across foils.

Nomenclature

C = chord length of hydrofoil C_T = instantaneous thrust coefficient C_P = instantaneous power coefficient C_Y = instantaneous lateral force coefficient \bar{C}_T = cycle-average thrust coefficient \bar{C}_P = cycle-average power coefficient

¹ Ph.D. student, <u>mns4zh@virginia.edu</u>, AIAA student member

² Ph.D., ph3gc@virginia.edu

³ Ph.D. student, <u>yp8xd@virginia.edu</u>

⁴ Professor, <u>haibo.dong@virgnia.edu</u>, AIAA Associate Fellow

cycle-average lateral force coefficient frequency of pitching oscillation gravitational acceleration vector moment or product of inertia unit vectors along x, y, and z axes

index of hydrofoil

 \vec{r} pressure acting on surface element

distance between pitching axis and a surface element on the solid

Re Reynolds number component of velocity u_i, u_i incoming flow speed \bar{T} cycle-average thrust

time elapsed t

components of space coordinate in cartesian grid x_i, x_i

propulsive efficiency

standard deviation of lateral force coefficient σ_{Y}

θ pitch angle fluid density ρ phase difference φ

vorticity (ı)

I. Introduction

In bio-inspired underwater propulsion, there has been a push towards understanding and emulating the multi-fin system exhibited by many fish species [1–4]. Large strides have been made towards proving the propulsive benefits of fin-fin interactions and unraveling the mechanisms behind such benefits, using fish-like models [5–7], or in-line foils to isolate the effect of the fins [8-15]. In a 2-dimensional (2-D) computational study, Akhtar et al. used 2 tandem foils with combined heaving and pitching motion based on the motion of median and caudal fins of the bluegill sunfish, to find the trailing foil's leading-edge vortex (LEV) enhanced through the capturing of the vortices shed by the foil upstream, and hence deriving a benefit in lift-based thrust production [11]. Boschitsch et al. used an experimental setup of two hydrofoils in-line undergoing pitching motion, and by varying the spacing between the two foils, the researchers found that the upstream foil can also derive a propulsive benefit when the two foils are placed less than 0.5 chord-length apart [8]. They also discovered two modes that the wake of the system of 2 tandem foils can settle into. Namely the coherent mode, where a single high-momentum jet is formed behind the trailing foil, and the branched mode, where two high-momentum jets split from the wake of the trailing foil. Kurt et al. used a similar experimental setup to study the 3-dimensional effects of the mechanisms previously discovered and found that the foil-foil interactions discovered in 2-D still qualitatively hold in 3-D [9]. Moreover, Kurt et al. discovered correlations of the coherent and branched modes to peak thrust and minimum power, respectively. Han et al., building upon the 2-foil setup, in a computational study, involved a third foil, and varied the phase differences between foils 1 and 2 and between foils 2 and 3 [10]. With the optimal combination of phase differences, the 3-foil system was able to outperform the 2-foil system. Through detailed flow-field analysis, they found the combinations of 2-P (paired) and 2-S (singular) vortices in the wake of the 3 tandem foils and discovered the benefit of the 2-P vortices in producing thrust jets effectively to produce branched jets.

Though the propulsive benefits of fin-fin interaction and the mechanism for their occurrence have been well studied by tandem foil studies, lateral force and stability analyses have been lacking in the community, despite evidence supporting the importance of such considerations from studies of fish swimming and underwater vehicle design [2,16– 18]. In studies of many fish species, the median fins are found to produce jets with substantial lateral components, indicating lateral force production [16–18], excessive amount of which can cause a fish to veer out of desired course. In a study of dorsal fin and anal fin functions by Standen and Lauder, it was found that the median fins' flapping and lateral jet shedding are timed such that the roll torque is minimized [18], demonstrating fish fins' important role in maintaining stability. However, in bio-inspired tandem foil studies, analysis of stability and lateral forces remains a gap. For underwater vehicles that employ a multi-fin system, though propulsive performance is important, lack of stability leading to control difficulties can result in loss of high propulsive performance. Therefore, the current study aims to examine lateral force and stability of a multi-fin system, using a tandem-foil configuration previously employed. Towards this end, a direct numerical simulation (DNS) solver will be used to solve Navier-Stokes (NS) equations, using similar simulation setup as described in Ref. [10,13] and similar tandem foil configuration described in Ref. [8–10,13]. In Section II., details of the simulation solver and setup will be described, and the results and analyses will be described in Section III.

II. Method

A. Configuration of Foils:

The current work studies an in-line 3-foil configuration, the same as previously encountered in the study conducted by Han et al. [10]. The foils share the same shape, including the rounded leading edges. They are placed uniformly a distance, s = 0.25 C, away from each other (head to tail), hinged at the leading-edge centers of arcs, C being the chord length of the foil. Each foil has 1 single degree of freedom (DOF), free to rotate around the pitching axis, but restricted from translating. The foils actively pitches periodically, based on prescribed sinusoidal function, given by Eq. 1, in which $\theta_1(t)$ is the pitch angle at time t, θ_0 is the maximum pitch angle, set as 7.56°, and f is the oscillating frequency in Hz, set to 1 Hz. The current combination of kinematics results in the Strouhal number (St) of 0.25. The Reynolds number (Re) used in the current study is 500.

$$\theta_1(t) = \theta_0 \cos(2\pi f \cdot t) \quad \theta_2(t) = \theta_0 \cos(2\pi f \cdot t + \phi_{2-1}) \quad \theta_3(t) = \theta_0 \cos[2\pi f \cdot t + \phi(2-1) + \phi_{3-2}]$$
 Eq. 1

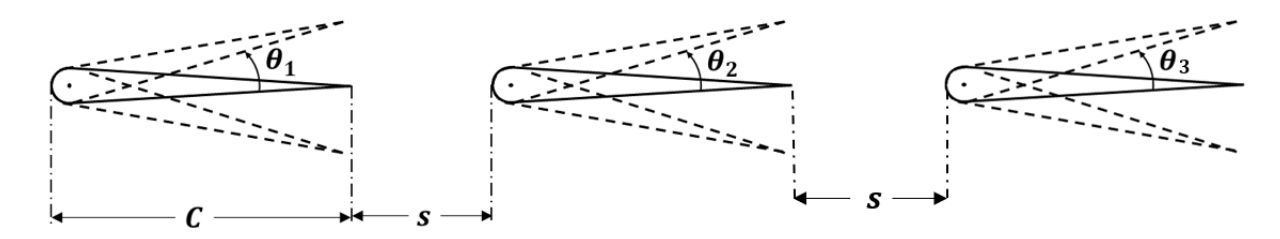


Fig. 1. The in-line configuration for the two identical foils, each with chord length, C, and between them a streamwise spacing, s.

B. The Numerical Solver

The numerical solver used in this study solves the unsteady incompressible viscous Navier-Stokes equations, shown in Eq. 2.

$$\frac{\partial u_i}{\partial x_i} = 0, \qquad \frac{\partial u_i}{\partial t} + \frac{\partial u_i u_j}{\partial x_j} = -\frac{\partial p}{\partial x_i} + \frac{1}{Re} \frac{\partial^2 u_i}{\partial x_i \partial x_j}$$
 Eq. 2

where u_i and u_i are components of velocity, p is pressure, and Re is the Reynolds number.

Equations 2 are discretized in space using a collocated Cartesian grid. The primitive variables, u_i and p, are both stored at cell centers, and solved using a second-order central difference method. On this grid, the foil boundaries are resolved using an immersed boundary method. For time stepping, a fractional step method is used to achieve second-order accuracy. The solver accuracy and detail has been described in detail in Ref. [19]. The computational grid employed here is the same as what has been used in Han et al. [10]. The solver using this combination of discretization methods has been applied in many simulations of biological and bio-inspired flapping and undulating motions [20–25].

III. Results and Discussion

The performance of each foil is quantified in terms of their thrust production, power consumption, propulsive efficiency, and lateral forcing, all of which are non-dimensionalized using Eq. 3. The coefficients, C_{T_j} , C_{P_j} and C_{Y_j} refer to the coefficients of thrust, power and lateral force (in the y-direction), and η_j is the propulsive efficiency for the *j*-th foil. The denominators for nondimensionalizing forces and power include the fluid density (ρ) , free-stream velocity (U_{∞}) and foil chord length (C)

$$C_{T_j} = \frac{T_j}{0.5\rho U_{\infty}^2 C^2}, \qquad C_{P_j} = \frac{P_j}{0.5\rho U_{\infty}^3 C^2}, \qquad C_{Y_j} = \frac{F_{Y_j}}{0.5\rho U_{\infty}^2 C^2}, \qquad \eta_j = \frac{C_{T_j}}{C_{P_j}}$$
 Eq. 3

The propulsive performance of the system over one entire typical pitching cycle can be quantified by taking the cycle-average values of coefficients of thrust and power to find \bar{C}_T , \bar{C}_P , and $\bar{\eta}$. Due to the lateral symmetry of the pitching motion, the cycle-average value of the lateral force, \bar{C}_Y , would be approximately zero, across all cases with varying lateral stability. The goal here is to analyze the amount of variation in the C_Y data in a flapping cycle. If the variation within the C_Y data is small, that means the system in forward propulsion experiences little lateral disturbances, and the system is stable. Conversely, the higher the variation in the C_Y cycle data, the less stable a system is. Toward this end, the standard deviation of C_Y is calculated and represented as σ_Y (Eq. 4), to account for the magnitude of variation or spread in the lateral force experienced by the multi-foil system over one pitching cycle. A large σ_Y would indicate substantial variation from cycle-average value (0) over a large portion of a cycle. This measure can be correlated to the lateral impulse, defined as the lateral force integrated over a time; a higher σ_Y can also lead to higher lateral impulse experienced by the system, more momentum exchanged between the flow and the foils, and therefore higher tendency to stray left or right.

$$\sigma_Y = \sqrt{\frac{\int_0^T [C_Y(t) - \bar{C}_Y]^2 dt}{T}}$$
 Eq. 4

The performance of the 3-foil system can be summarized by Fig. 2. Figure 2 (a) and (b) are familiar results encountered in Han et al. [10], and Fig. 2 (c) is the result of the current lateral-force spread analysis. While the propulsive force and efficiency contours have similar groupings of high performing (located around (ϕ_{2-1}, ϕ_{3-2})) = (300°, 320°)) and low performing (located around ϕ_{2-1} , $\phi_{3-2} = (180^\circ, 150^\circ)$), σ_Y contour has a unique trend that differs from the other two. Some striking features of the σ_Y contour plot are the following. 1. The corners are occupied by high values of σ_{v} , indicating large amount of variation in the lateral force over one flapping. The cases occupying the corners have foils that are similar in phase, causing the side forces of the foils to accumulate. The system that experienced the absolute highest σ_Y has all 3 foils in phase, $(\phi_{2-1}, \phi_{3-2}) = (360^\circ, 360^\circ)$, where $\sigma_Y = 4.20$, and the propulsive performance is near the peak [10], $\bar{C}_T = 0.174$. 2. Diagonal symmetries are exhibited, indicating lateralforce oscillation similarities between cases with similar magnitudes of phase differences among its constituting foils, but with different foils in lead and lag. 3. Two local minima of lateral force oscillations are observed close to the 1/3 and 2/3 division points along the diagonal, indicating that in the current 3-foil system, the optimal lateral stability is achieved when the phases differences $(\phi_{2-1}, \phi_{3-2}, \phi_{1-3})$ are roughly evenly distributed. An extension of this hypothesis of evenly distributed phase differences leading to optimal stability can be raised for the inclusion of more foils. The exact locations of the local minima in the phase contour plot are $(\phi_{2-1}, \phi_{3-2}) = (150^\circ, 120^\circ)$, and $(\phi_{2-1}, \phi_{3-2}) = (210^\circ, 240^\circ)$. The two have similar magnitudes of phase differences. Whereas in the $(150^\circ, 120^\circ)$ case, foil 1 lags foil 2, and foil 2 lags foil 3 in phase, in the (210°, 240°) case, foil 1 leads foil 2, and foil 2 leads foil 3 in phase. At $(150^\circ, 120^\circ)$, $\sigma_Y = 0.56$, and at $(210^\circ, 240^\circ)$, $\sigma_Y = 0.47$. The case with the trailing foils lagging in phase compared to the leading foils perform slightly better than the case with the trailing foils leading in phase, in terms of lateral stability.

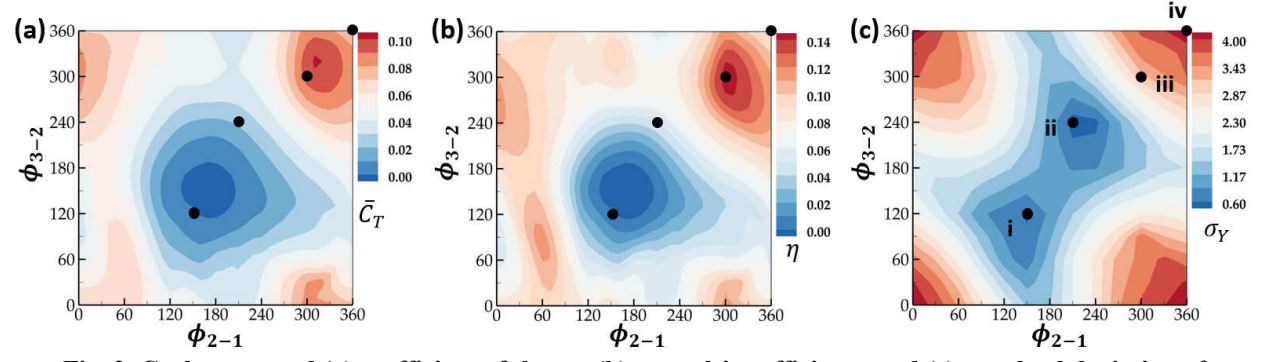


Fig. 2. Cycle-averaged (a) coefficient of thrust, (b) propulsive efficiency and (c) standard deviation of coefficient of lateral force.

To examine the flow physics involved in the generation of large side force and its minimization, four cases are selected for closer examination, including (i and ii) the two σ_Y local minima, (iii) the case at (300°, 300°) with

mediocre lateral stability and excellent thrust production, and (iv) the case with the worst lateral stability performance and mediocre thrust production, at (360°, 360°). These cases are labeled i-iv in Fig. 2 (c), and their locations on the phase contour plots are indicated in Fig. 2 (a-c).

The instantaneous C_Y over one typical cycle is plotted in Fig. 3. Each individual foil follows a sinusoidal curve that completes one cycle per flapping cycle of the system, and the magnitude of an individual-foil curve varies little within a case and across all cases, showing that the foils 1, 2 and 3 experience similar amount of lateral forces across all cases. The main difference exhibited by the individual-foil curves is the locations of the peaks within a cycle, or the relative flapping phase differences among the foils. Combinations of foil phases within a case can lead to drastic differences in system performance in terms of lateral forces. Foil 1 has the same phase across all cases, agreeing well with Eq. 1. The other two foils exhibit different combinations of phases in different cases. In case iv, $\phi_{2-1} = \phi_{3-2} =$ 0, and therefore all three curves are overlapped on top of each other (Fig. 3 (d)), leading to its detriment. Due to the concurrence of peak lateral forces on all three foils in case iv, the system sum drastically exceeds individual values at the peak. In case iii, though the foils are not flapping exactly in phase, due to the phase difference still being relatively small, the system sum still experiences a large sinusoidal oscillation with an amplitude that is higher than each individual foil (Fig. 3 (c)), though smaller than the system sum of case iv. Conversely, cases i and ii (Fig. 3 (a, b)) show the effect of optimal phase configurations leading to a desired decrease of system sum oscillation amplitude. The key observation that distinguishes cases i and ii from cases iii and iv is the equal spacing of all 3 peaks in Fig. 3 (a, b), i.e., $\phi_{2-1} \approx \phi_{3-2} \approx \phi_{1-3}$. Equal spacing of phases of sine wave is conducive to cancellation when summed together, under the premise that the sine waves all have the same amplitude. Figure 3 (a) shows a decrease of C_V peaks in non-leading foils. Though this can mean less lateral forcing oscillation, and therefore better stability for the individual foils, this leaves the large lateral force amplitudes of foil 1 unopposed, raising the overall amplitude, as evidenced by the comparison between the case i and ii (Fig. 3 (a, b)). The equal spacing of flapping phases in case ii, and the relatively equal lateral force magnitudes among individual foils in case iii, leads to the optimal cancellation of lateral force and ultimately it having the overall lowest σ_{V} .

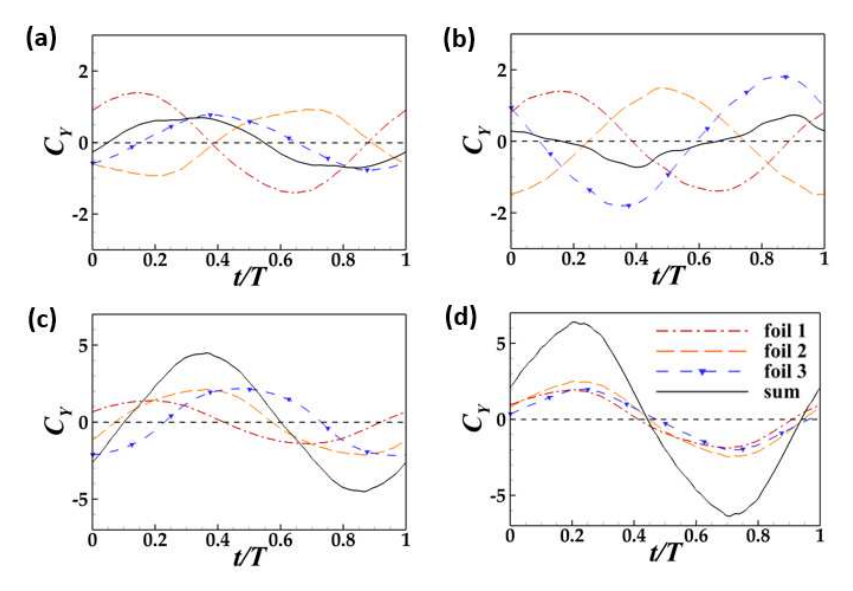


Fig. 3. Instantaneous coefficient of lateral force of (a) case i: $(\phi_{2-1}, \phi_{3-2}) = (150^\circ, 120^\circ)$, (b) case ii: $(\phi_{2-1}, \phi_{3-2}) = (210^\circ, 240^\circ)$, (d) case iv: $(\phi_{2-1}, \phi_{3-2}) = (300^\circ, 300^\circ)$, (d) case iv: $(\phi_{2-1}, \phi_{3-2}) = (360^\circ, 360^\circ)$

To examine the hydrodynamics of cases i-iv, the mean flow and vortex structure in foil wake are visualized in Fig. 4. The mean flow is calculated by averaging flow velocity over several flapping cycles. Regions with dense colors indicate areas where the flow exhibits a high amount of momentum over one flapping cycle, indicating strong jets formed in direction signified by the color, leading to force production in the opposite direction. Wake vortices are grouped and labeled, and key vortices that are responsible for lateral force production are labeled in Fig. 4 (b1-b3) following the conventions set by Han et al. [10]. Briefly, vortices that originate from foils 1, 2, and 3 are labeled with letters A, B and C respectively. The number following the letter indicates if the vortex is shed at the leading edge (A1, B1, C1) or the trailing edge (A2, B2, C2). Apostrophes, when applicable, indicate the vortex from the previous half

cycle. Due to the kinematic and geometric symmetry, the vortex shedding analysis will focus on just the left side of the foils, while the vortices on the right side follow similar trends but with mirrored dynamics.

The mean flow shows thrust jets in the wake of all four cases, with the jet in case i being the weakest, corresponding to its low thrust production. Both case i and ii have singular jets directly behind the trailing foil formed due to the well-ordered 2-S, reverse von-Kármán vortical streets, whereby 2 counter-rotating vortices are generated per cycle, conveying the flow backward. Instead of singular coherent jets, the time-average velocity contours of cases iii and iv show branched jets (Fig. 4 (a3, a4)), with transitional 2-P wake (t2-P) found in case iii, whereby, 2 vortex pairs are formed per flapping cycle. In Han's study, the 2-P wakes are linked to high propulsive performance [10], which holds true in the current study. The vortex pairs labeled in Fig. 4 (b3), effectively generate jets (labeled by green arrows) with strong backward components. The wake region directly behind the trailing foil in Fig. 4 (b3), disregarding the edge vortices in the t2-P pairs, shows vortices in a von-Kármán Street, corresponding to the reduced flow speed in the region between the two branched jets.

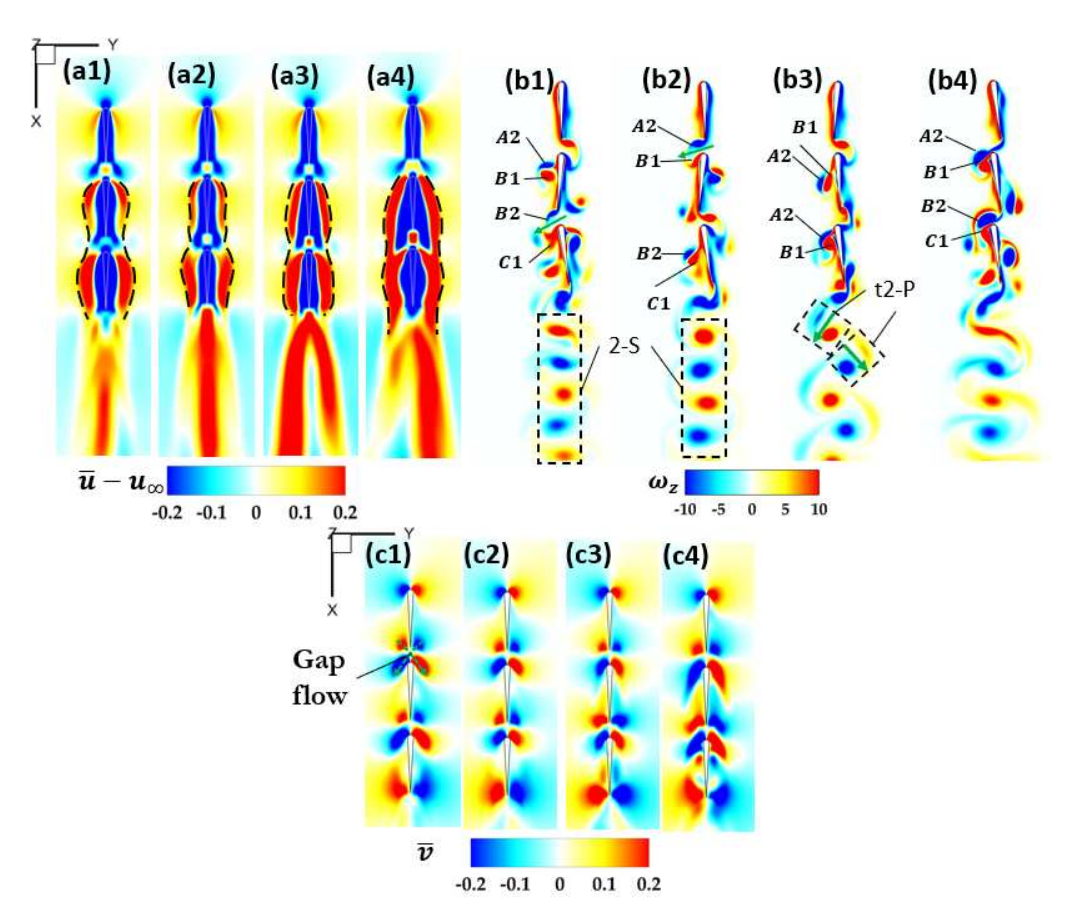


Fig. 4. Visualization of flow showing (a) contour of stream-wise component of mean flow velocity with the free-stream velocity subtracted, with the envelope of high-momentum region near the foils traced out with dashed lines, (b) the vorticity contour and (c) the cross-stream component of mean flow velocity for (a1, b1, c1) case i, (a2, b2, c2) case ii, (a3, b3, c3) case iii, and (a4, b4, c4) case iv, as labeled in Fig. 2.

Though 2-P wakes and branched jets have been linked to high propulsive performance, but the current comparison provides evidence that they can also be linked to increased oscillation of lateral force, leading to instability, as jet branching is observed in the non-optimal cases, in which the system sum of lateral force oscillation has larger amplitudes than the individual foils. The optimal cases, cases in which the individual-foil lateral forces tend to cancel out and result in a system sum that has lower amplitude than an individual foil, exhibit singular, coherent jets and 2-S vortical wakes. Tracing upstream, the envelopes of high-momentum regions near the foils are observed, as labeled in in Fig. 4 (a). A general trend of growing intensity and width of the high-momentum region is observed, due to the acceleration of the flow with each additional foil. Also, varying degrees of diverging and converging can be observed around each foil. Near the leading edge of a foil, flow is deflected outwards, and due to the flapping of the foil, the

flow is drawn back in towards the foil centerline and accelerated downstream, as evidenced by the cross-stream timeaverage velocity contour shown in Fig. 4 (c1-c4), causing the high-momentum envelope to first diverge near the leading edge and then converge slowly towards the trailing edge. This is especially clear in the optimal cases i and ii. Comparatively, though diverging of the envelopes at the leading edges of foils 2 and 3 are clearly seen in cases iii and iv, the convergence of the envelope is weaker. Instead, cases iii and iv have high-momentum envelopes that "flare out," indicating high momentum dispensed in the lateral directions. The "flaring out" of the high-momentum envelopes of case iv also causes the width of the envelopes to be significantly larger than that of the optimal cases, indicating again high lateral momentum exchanged between the flow and the foil. Corresponding to this, the contour plots of the lateral components of the velocity time average shows the flow around foils 2 and 3 in case iv as having stronger lateral flow (Fig. 4 (c4)). Also shown in Fig. 4 (c) is the formation of jets in the gaps between the trailing edge of a leading foil and the leading edge of a trailing foil. The gap flow directions are labeled in Fig. 4 (c1). These gap flows can be linked to vortex pairs composed of the trailing-edge vortex and the leading-edge vortex (TEV and LEV) of the leading and trailing foils, respectively. In the gap between foil 1 and 2, the counter rotating A2 and B1 together can form a lateral jet, as shown in Fig. 4 (b2). A2 and B1, when combined, form a pair and are advected downstream together, as seen in Fig. 4 (b1, b3, b4). Similarly, between foil 2 and 3, B2 and C1 can produce a lateral jet in the space between them, as shown in Fig. 4 (b1, b4), and the advection of this vortex pair is shown in Fig. 4 (b2, b3). When actively being formed, still attached to their respective foils, the vortex pair creates jets (green arrows in Fig. 4 (b1, b3)) resembling gap flows (Fig. 4 (c1)). It is therefore determined that the formation of LEV-TEV vortex pair in the gap between two foils is crucial to the generation of lateral force in a multi-foil system.

Next the individual foil's vortex forming, and shedding is examined and linked to lateral-stability performance. Of the optimal case of $(\phi_{2-1}, \phi_{3-2}) = (210^\circ, 450^\circ)$, moments when C_{Y_i} is at a maximum and when $C_{Y_i} = 0$ are shown in Fig. 5. At the instant when foil 1's C_Y is at a maximum, depicted in Fig. 5 (a1), the foil is at a shallow angle relative to the incoming stream, and its TEV, A2 is just beginning to form. At the instant when foil 1's C_Y crosses 0, depicted in Fig. 5 (a2), the previously formed A2 begins to shed and be advected towards foil 2. Similarly, at foil 2's peak- C_Y moment, at the trailing edge, B2 is starting to form (Fig. 5 (a1)), which is shed at the moment when foil 2's C_Y crosses 0, as shown in Fig. 5 (b2). At the instant depicted in Fig. 5 (b1), the TEV shed by foil 1 from the previous half cycle, A'2, and the LEV shed by foil 2 from the previous half cycle, B'1, can be seen forming a pair of counter rotating vortices, creating a laterally facing jet that points to the left. In this vortex pair, foil 2's LEV, B'2 dominates, and imposes an overall counter-clockwise torque on the pair. As a result, at a later depicted instant, in Fig. 5 (b2), the vortex pair has been rotated counterclockwise compared to the previous timestep. At the new orientation, the et created by the vortex pair has a stronger streamwise component, conducive to thrust production. This rotation of vortex pair towards stream-wise direction corresponds well with the narrowing of the high-momentum envelope observed in Fig. 4 (a2). Foil 3 follows a similar trend.

Now, a general observation can be made that coinciding with an individual foil's C_Y peaking is the initiation of the trailing-edge vortex of the said foil, and when the trailing-edge vortex is beginning to shed, similarly relieved is the foil's C_Y , as its magnitude reaches 0. This correlates well with the pressure distribution. At the moment of peak C_Y , depicted for each individual foil in Fig. 5 (d1, e1, f1), there is a buildup of pressure potential, and the flow has nowhere to go but around individual foils. The pressure then acts on the individual foil to create a lateral-facing force, leading to the high C_{Yi} observed in these instants. The pressure potential induces a flow laterally around the trailing edge of a foil, and thus initiating the formation of a trailing-edge vortex, as indicated by the green arrows in Fig. 5 (d1, e1, f1). Associated with the vortex, a low-pressure region is also created, as indicated in Fig. 5 (d1). The cross-stream flow in the gaps, aided by the trailing-edge vortices provides relief to the pressure buildup. As a result, as Fig. 5 (d2, e2, f2) show, the large pressure gradient previously observed in Fig. 5 (d1, e1, f1) is no longer observed. Corresponding to the shed trailing-edge vortices at the instants of $C_{Yi} = 0$, shown in Fig. 5 (a2, b2, c2), in Fig. 5 (d2, e2, f2), low-pressure regions created by the TEVs are also advected downstream.

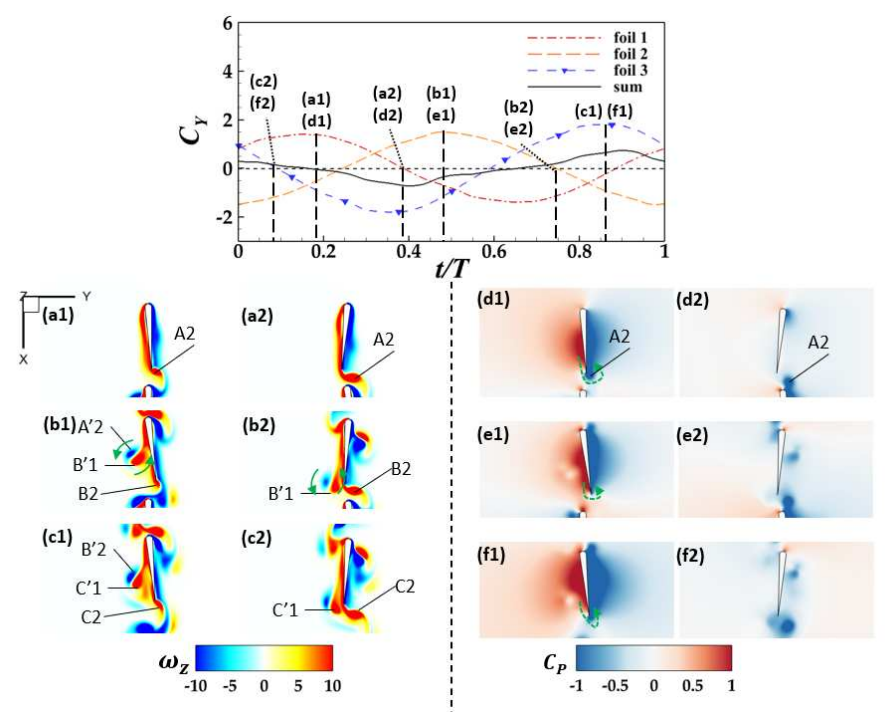


Fig. 5. (a-c) Instantaneous vorticity contour and (d-f) pressure contour for (a1, a2, d1, d2) foil 1, (b1, b2, e1, e2) foil 2, and (c1, c2, f1, f2) foil 3, at instants of (a1, b1, c1, d1, e1, f1) peak C_{Y_i} , where i indicates the foil plotted, and instants of (a2, b2, c2, d2, e2, f2) $C_{Y_i} = 0$ for the optimal case of $(\phi_{2-1}, \phi_{3-2}) = (210^\circ, 450^\circ)$.

The pressure contour plots of the cases at instants of peak system sum lateral force, shown in Fig. 6, highlights the disadvantage of in-phase configurations of tandem pitching foils in terms of lateral stability. Fig. 6 (d) (case iv) stands out from the other cases as having high pressure buildup on the left side, and high suction buildup on the right side of the three foils. Case iii is an improvement from case iv in varying the foil flapping phases to allow pressure gradients to be released through the gaps that are widened due to phase shift. However, the phase differences are still not optimal, as seen by the buildup of pressure potential around foil 2 and 3. Cases i and ii demonstrate further improvements. At each moment the gaps between adjacent foils are maximized in cases i and ii, leaving the largest possible gaps to allow fluid to escape from high pressure region to low pressure region, and thus avoiding the buildup of large pressure potential that can apply large lateral force on the system. In case iv, the gaps between the foils are minimized when the foils are aligned, preventing pressure-driven flow, and causing pressure to build up. As a result, the peak lateral force of case iv drastically exceeds those of case i and case ii. Cases i and ii can achieve minimum lateral force oscillation owing to the coordination of the opening and closing of gaps to allow flow to neutralize pressure gradient buildup.

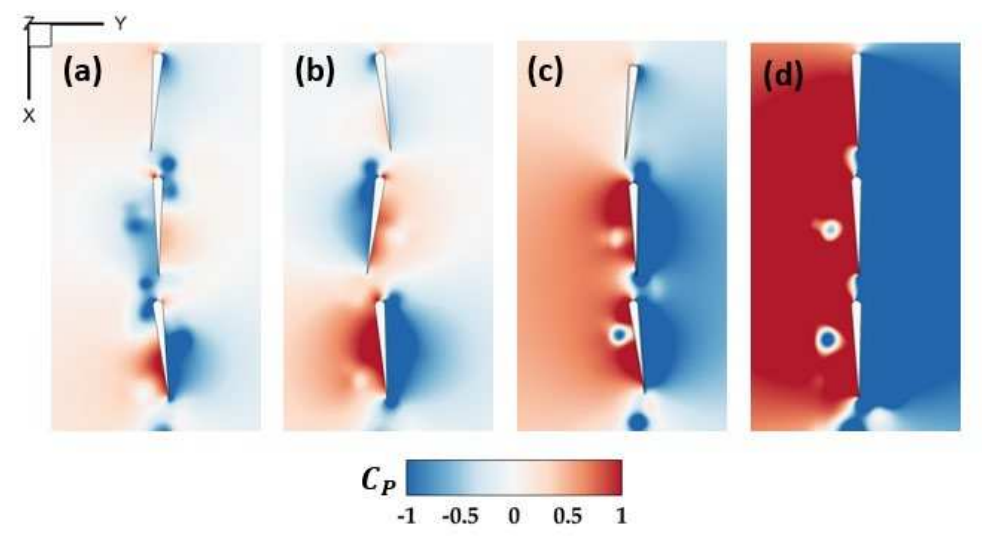


Fig. 6. Pressure contour of the cases i, ii, and iii at a moment of peak lateral force (a) case i at t/T = 0.34, (b) case ii at t/T = 0.91 (c) case iii at t/T = 0.375, and (d) case iv at t/T = 0.22

IV. Conclusion

In this study, a classic case of three tandem foils undergoing pitching motion is revisited from the angle of lateral stability. The lateral stability is quantified in this study as the standard deviation of the lateral force cycle data, σ_V , to account for the variation, or spread, in the lateral force experienced by the system over one entire flapping cycle. A system with a higher σ_Y , or more variation in its lateral force history, is said to be less stable, as it receives higher amount of disturbing lateral impulses. With this definition, by varying the flapping phase differences between foil 1 and 2 and between 2 and 3, it is found that the lateral stability is optimized when the phases of the 3 foils are equally spaced. Specifically, two local minima are found at $(\phi_{2-1}, \phi_{3-2}) = (150^\circ, 120^\circ)$, and $(\phi_{2-1}, \phi_{3-2}) = (150^\circ, 120^\circ)$ (210°, 240°), with the latter being the global minimum of lateral force variation. The worst performing case is with the three foils all in phase. Whereas the individual foil lateral forces would compound to lead to a system sum that is many times the individual value in the worst performing case, the optimal case has the three foils perfectly out of phase to cancel out each other's oscillation. Though previously 2-P wakes have been linked to desirable high propulsive performance, in this study, evidence is observed for systems with 2-P wakes to experience undesirable high lateral force oscillations. The time-average flow contours show regions of high stream-wise momentum. With the envelope of such regions near the foils traced out, it is seen that high lateral oscillations are linked with wide and flaring-out high-momentum envelopes, whereas the optimal systems exhibit narrower, and diverging-converging high-momentum envelopes. The cross-stream time-average velocity contour shows the existence of the gap flow in the space between the trailing edge and leading edge of two consecutive foils. The gap flow strength is linked to the lateral jets that are produced by the TEV and LEV of two consecutive foils. It is found that when a foil experiences high lateral force, high pressure differential builds up across the foil that induces a flow around a foil's trailing edge and initiates a TEV. At moments when an individual foil's lateral force crosses 0, the TEV begins to separate. The shed TEV then encounters the following foil's LEV, causing it to shed, and the pair produces a lateral jet that is indicative of high amount of lateral momentum exchanged between the flow and the foil.

Through this study, lateral stability of a tandem pitching foil system is linked to the flow in the gap between two foils. The peak and neutrality instants of lateral force of an individual foil are linked to the initiation and the shedding of the TEV of the said foil. The cause of high lateral force oscillation is established to be the build-up of pressure gradient across the foil system, due to a lack of adequate opening between consecutive foils. The gap flow observed in the time-average cross-stream velocity contour, and the TEV formation are all caused by the build-up of pressure gradient, and therefore good indicators of lateral stability. However, more quantitative flow analyses need to be conducted on more individual cases on the σ_Y contour before the roles of gap flow and TEV in maintaining lateral stability in a tandem-foil system can be determined.

Acknowledgements

Thanks to the University of Virginia Research Computing Group for the availability of the Rivanna supercomputing cluster. This research was supported by grants from the Office of Naval Research (N00014-14-1-0533 and N00014-15-1-2234), and CNS-1931929 to HD.

References

- [1] Zhu, J., White, C., Wainwright, D. K., Santo, V. di, Lauder, G. V., and Bart-Smith, H. *Tuna Robotics: A High-Frequency Experimental Platform Exploring the Performance Space of Swimming Fishes*. 2019.
- [2] Lauder, G. V., and Madden, P. G. A. Learning from Fish: Kinematics and Experimental Hydrodynamics for Roboticists. 2006.
- [3] Lauder, G. V., Madden, P., Hunter, I., Tangorra, J., Davidson, N., Proctor, L., Mittal, R., Dong, H., and Bozkurttas, M. Design and Performance of a Fish Fin-like Propulsor for AUVs. 2005.
- [4] Narasimhan, M., Dong, H., Mittal, R., and Singh, S. N. "Optimal Yaw Regulation and Trajectory Control of Biorobotic AUV Using Mechanical Fins Based on CFD Parametrization." *Journal of Fluids Engineering*, Vol. 128, No. 4, 2006, pp. 687–698. https://doi.org/10.1115/1.2201634.
- [5] Han, P., Lauder, G. V., and Dong, H. "Hydrodynamics of Median-Fin Interactions in Fish-like Locomotion: Effects of Fin Shape and Movement." *Physics of Fluids*, Vol. 32, No. 1, 2020. https://doi.org/10.1063/1.5129274.
- [6] Liu, G., Ren, Y., Dong, H., Akanyeti, O., Liao, J. C., and Lauder, G. V. "Computational Analysis of Vortex Dynamics and Performance Enhancement Due to Body-Fin and Fin-Fin Interactions in Fish-like Locomotion." *Journal of Fluid Mechanics*, Vol. 829, 2017, pp. 65–88. https://doi.org/10.1017/jfm.2017.533.
- [7] Matthews, D. G., and Lauder, G. V. "Fin-Fin Interactions during Locomotion in a Simplified Biomimetic Fish Model." *Bioinspiration and Biomimetics*, Vol. 16, No. 4, 2021. https://doi.org/10.1088/1748-3190/ac03a8.
- [8] Boschitsch, B. M., Dewey, P. A., and Smits, A. J. "Propulsive Performance of Unsteady Tandem Hydrofoils in an In-Line Configuration." *Physics of Fluids*, Vol. 26, No. 5, 2014. https://doi.org/10.1063/1.4872308.
- [9] Kurt, M., and Moored, K. W. "Flow Interactions of Two- and Three-Dimensional Networked Bio-Inspired Control Elements in an in-Line Arrangement." *Bioinspiration and Biomimetics*, Vol. 13, No. 4, 2018. https://doi.org/10.1088/1748-3190/aabf4c.
- [10] Han, P., Pan, Y., Liu, G., and Dong, H. "Propulsive Performance and Vortex Wakes of Multiple Tandem Foils Pitching In-Line." *Journal of Fluids and Structures*, Vol. 108, 2022. https://doi.org/10.1016/j.jfluidstructs.2021.103422.
- [11] Akhtar, I., Mittal, R., Lauder, G. V., and Drucker, E. G. "Hydrodynamics of a Biologically Inspired Tandem Flapping Foil Configuration." *Theoretical and Computational Fluid Dynamics*, Vol. 21, No. 3, 2007, pp. 155–170. https://doi.org/10.1007/s00162-007-0045-2.
- [12] Triantafyllou, M. S., Techet, A. H., and Hover, F. S. "Review of Experimental Work in Biomimetic Foils." *IEEE Journal of Oceanic Engineering*, Vol. 29, No. 3, 2004, pp. 585–594. https://doi.org/10.1109/JOE.2004.833216.
- [13] Yuan, C., Liu, G., Ren, Y., and Dong, H. Propulsive Performance and Vortex Interactions of Multiple Tandem Foils Pitching in Line. 2015.
- [14] Hegde, A. S., Gurugubelli, P. S., and Joshi, V. "Effect of Combined Heaving and Pitching on Propulsion of Single and Tandem Flapping Foils." 2022.
- [15] Bozkurttas, M., Dong, H., Seshadri, V., Mittal, R., and Najjar, F. Towards Numerical Simulation of Flapping Foils on Fixed Cartesian Grids. 2005.
- [16] Drucker, E. G., and Lauder, G. v. "Locomotor Function of the Dorsal Fin in Teleost Fishes: Experimental Analysis of Wake Forces in Sunfish." *Journal of Experimental Biology*, 2001, pp. 2943–2958.
- [17] Drucker, E. G., and Lauder, G. V. "Locomotor Function of the Dorsal Fin in Rainbow Trout: Kinematic Patterns and Hydrodynamic Forces." *Journal of Experimental Biology*, Vol. 208, No. 23, 2005, pp. 4479–4494. https://doi.org/10.1242/jeb.01922.
- [18] Standen, E. M., and Lauder, G. V. "Hydrodynamic Function of Dorsal and Anal Fins in Brook Trout (Salvelinus Fontinalis)." *Journal of Experimental Biology*, Vol. 210, No. 2, 2007, pp. 325–339. https://doi.org/10.1242/jeb.02661.
- [19] Zhang, W., Pan, Y., Wang, J., Santo, V. di, Lauder, G. v, and Dong, H. An Efficient Tree-Topological Local Mesh Refinement on Cartesian 1 Grids for Multiple Moving Objects in Incompressible Flow 2.

- [20] Khalid, M. S. U., Wang, J., Dong, H., and Liu, M. "Flow Transitions and Mapping for Undulating Swimmers." *Physical Review Fluids*, Vol. 5, No. 6, 2020, p. 063104. https://doi.org/10.1103/PhysRevFluids.5.063104.
- [21] Li, C., Dong, H., and Zhao, K. "A Balance between Aerodynamic and Olfactory Performance during Flight in Drosophila." *Nature Communications*, Vol. 9, No. 1, 2018, p. 3215. https://doi.org/10.1038/s41467-018-05708-1.
- [22] Bode-Oke, A. T., Zeyghami, S., and Dong, H. "Aerodynamics and Flow Features of a Damselfly in Takeoff Flight." *Bioinspiration and Biomimetics*, Vol. 12, No. 5, 2017. https://doi.org/10.1088/1748-3190/aa7f52.
- [23] Ren, Y., Dong, H., Deng, X., and Tobalske, B. Turning on a Dime Asymmetric Vortex Formation in Hummingbird Maneuvering Flight. 2015.
- [24] Pan, Y., and Dong, H. "Effects of Phase Difference on Hydrodynamic Interactions and Wake Patterns in High-Density Fish Schools." *Physics of Fluids*, Vol. 34, No. 11, 2022, p. 111902. https://doi.org/10.1063/5.0113826.
- [25] Pan, Y., and Dong, H. "Computational Analysis of Hydrodynamic Interactions in a High-Density Fish School." *Physics of Fluids*, Vol. 32, No. 12, 2020, p. 121901. https://doi.org/10.1063/5.0028682.